Design and assessment of a novel SPECT system for desktop open-gantry imaging of small animals: A simulation study

Navid Zeraatkar and Mohammad Hossein Farahani
Research Center for Molecular and Cellular Imaging, Tehran University of Medical Sciences, Tehran 1419733141, Iran

Arman Rahmim
Department of Radiology, Johns Hopkins University, Baltimore, Maryland 21287 and Department of Electrical and Computer Engineering, Johns Hopkins University, Baltimore, Maryland 21218

Saeed Sarkar
Department of Medical Physics and Biomedical Engineering, Tehran University of Medical Sciences, Tehran 1417613151, Iran and Research Center for Science and Technology in Medicine, Tehran University of Medical Sciences, Tehran 1419733141, Iran

Mohammad Reza Ay[a)]
Research Center for Molecular and Cellular Imaging, Tehran University of Medical Sciences, Tehran 1419733141, Iran and Department of Medical Physics and Biomedical Engineering, Tehran University of Medical Sciences, Tehran 1417613151, Iran

Purpose: Given increasing efforts in biomedical research utilizing molecular imaging methods, development of dedicated high-performance small-animal SPECT systems has been growing rapidly in the last decade. In the present work, we propose and assess an alternative concept for SPECT imaging enabling desktop open-gantry imaging of small animals.

Methods: The system, PERSPECT, consists of an imaging desk, with a set of tilted detector and pinhole collimator placed beneath it. The object to be imaged is simply placed on the desk. Monte Carlo (MC) and analytical simulations were utilized to accurately model and evaluate the proposed concept and design. Furthermore, a dedicated image reconstruction algorithm, finite-aperture-based circular projections (FABCP), was developed and validated for the system, enabling more accurate modeling of the system and higher quality reconstructed images. Image quality was quantified as a function of different tilt angles in the acquisition and number of iterations in the reconstruction algorithm. Furthermore, more complex phantoms including Derenzo, Defrise, and mouse whole body were simulated and studied.

Results: The sensitivity of the PERSPECT was 207 cps/MBq. It was quantitatively demonstrated that for a tilt angle of 30°, comparable image qualities were obtained in terms of normalized squared error, contrast, uniformity, noise, and spatial resolution measurements, the latter at ~0.6 mm. Furthermore, quantitative analyses demonstrated that 3 iterations of FABCP image reconstruction (16 subsets/iteration) led to optimally reconstructed images.

Conclusions: The PERSPECT, using a novel imaging protocol, can achieve comparable image quality performance in comparison with a conventional pinhole SPECT with the same configuration. The dedicated FABCP algorithm, which was developed for reconstruction of data from the PERSPECT system, can produce high quality images for small-animal imaging via accurate modeling of the system as incorporated in the forward- and back-projection steps. Meanwhile, the developed MC model and the analytical simulator of the system can be applied for further studies on development and evaluation of the system. © 2016 American Association of Physicists in Medicine.
[http://dx.doi.org/10.1118/1.4947127]

1. INTRODUCTION

Given the increasing role of molecular SPECT imaging in preclinical research in the past decade, much effort has been dedicated to develop appropriate instrumentation for high-performance SPECT imaging systems.[1] Position-sensitive photomultipliers (PSPMTs) have been interesting devices for detection and positioning of the light produced by scintillator crystals in the field of small-animal imaging due to their high spatial resolution.[2–8] Meanwhile, application of solid-state detectors for small-animal imaging has become an option for its ultrahigh energy resolution, high spatial resolution, good detection efficiency, in addition to its capability for developing compact detectors and suitable radiation collimation.[9] There are several examples of the systems applied solid-state detectors or semiconductor detectors coupled to

scintillator crystals.[10–13] Some other creative techniques like oversampling,[14] skew-slit or slit-aperture collimators,[15,16] and pinhole/multipinhole collimators[17,18] have also been utilized in development of small-animal SPECT imaging systems. However, almost all of the systems have been conventionally based on mounting the set of collimators/detectors on a rotating gantry. The gantry then rotates around the object to be imaged to acquire projection data in different views, leading to a closed-gantry configuration. Even in the creative case of stationary SPECT systems,[19–24] the rotation of detectors has been replaced by implementation of numerous pinholes around the object which still form a closed-gantry configuration. To the best of our knowledge, no small-animal SPECT system with completely open-gantry structure has been developed so far, though the following two works provided pseudo-open-gantry configurations. A stationary dual-headed system for small-animal SPECT was developed providing access to the object to be imaged from all but two sides.[25] In another work, the concept of synthetic collimation was used to form a small-animal imaging in a single tomographic angle configuration.[26] Still, similar to the previous work, the gantry imaging configuration was not completely open.

In the present work, we developed an innovative concept for data acquisition and image reconstruction in SPECT that can be especially utilized for dedicated small-animal imaging. The new system called PERSPECT (new PERSPECTive in SPECT) does not involve a conventional gantry and enables desktop open-gantry imaging of small animals.

The open feature of the system enables the user to easily monitor the animal during the scan visually (taking into account radiation protection regulations) or by attaching devices for electronically measuring the temperature, heart rate, etc. The application of anesthesia equipment will also be simple. Furthermore, nonrestrained/nonanesthetized animal imaging is expected to be more feasible, given better ability to track motion and its various degrees of freedom.[27–29]

Monte Carlo (MC) simulation in the field of medical imaging and nuclear medicine is an important tool[30] in design and development,[31–33] performance evaluation,[34,35] and correction and optimization[24,36–39] of systems. Despite the accuracy and reliability of MC modeling, it is a time-consuming approach in simulating the process of data acquisition in a medical imaging system, e.g., SPECT or PET. Even with cost-effective high computational power, time allocated to each round of simulations may be too long in case of complicated systems and high-resolution voxelized phantoms, etc. An alternative to MC simulation is analytical simulation in which the process of the transport of the particle/photon from the emitting source to the detector is modeled through analytical operators. Although the accuracy of analytical simulations may be less than MC simulations, increasingly accurate methods can be utilized, while providing much faster simulations. As an example, Mok et al.[40] developed an analytical simulator to model focusing multipinhole projections and to assess the effects of multiplexing in multipinhole small-animal SPECT. Two different types of digital phantoms, mouse whole body phantom (MOBY) and a hot sphere phantom, were used for the simulations. Poisson noise was added to the projections to generate noisy data sets.

In addition, Zhang and Qi[41] developed an analytical method to model the process of image formation in cone-beam CT and pinhole SPECT imaging. A ray-tracing method for cone-beam CT and voxel-driven method for pinhole SPECT were applied together including modeling of resolution degradation. A variety of digital phantoms including 3D Shepp-Logan phantom, Jaszczak phantom, and Defrise phantom were used in the simulations. The analytically simulated results were in accordance with the ones in practical experiments. Also, Vaissier et al.[42] used analytical simulations to model and simulate an animal SPECT system with stationary gamma cameras and focusing multipinhole collimators. The analytical simulator was applied to precalculate the system matrix by simulating point sources in addition to generating phantom projection data. Poisson statistics were used to emulate the noise regarding the administered activity and scan time. In a similar way, Aguiar et al.[43] compared the effect of using analytical and MC simulations for calculating the system response matrix on the reconstructed images in a pinhole SPECT system. A hot cylinder phantom and a custom-made Derenzo phantom were applied for assessment. The authors demonstrated that the system response matrix obtained by the analytical simulator was faster and handled noise better than the one using MC simulations. Both methods were declared as good solutions for calculating the system response matrix.

In the present work, we introduce and elaborate upon the proposed system together with appropriate image reconstruction algorithm developed for the system. First, the preliminary evaluation of the system using point sources or simple phantoms is presented, wherein MC modeling using GEANT4 application for tomographic emission (GATE) (Refs. 44 and 45) was utilized. Also, the impact of tilt angle in data acquisition and number of iterations in image reconstruction on image quality were analyzed using MC data. Then, an analytical simulator developed for simulation of the performance of the system is described, and utilized given its high speed in comparison to MC simulations, and more complicated phantoms, e.g., Derenzo, Defrise, and MOBY phantoms[46] were simulated as such and the results were reported.

2. MATERIALS AND METHODS

2.A. The concept and design of the system

The main novelty in the design concept of the PERSPECT is the data acquisition protocol and movement of the system. The majority of current SPECT systems are based on a table or a bed (often with translational movement to be able to enter/exit the gantry) for placing the object together with a gantry. The gantry then rotates around a circular path on a plane perpendicular to the table in a step-and-shoot manner to acquire projection data in different views. By contrast, our design concept is based on a desk, along with a tilted gamma camera head and a collimator. Pinhole collimation is used to provide both high resolution and appropriate sensitivity for the required field-of-view (FOV) in small-animal imaging. As illustrated in Fig. 1(a), the detector/collimator pair (the head) is located underneath the desk. As such, the final product from
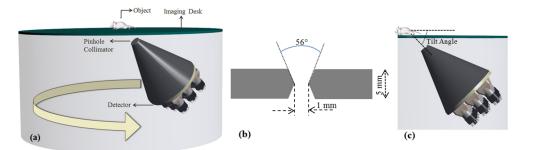
FIG. 1. (a) Conceptual illustration of the system showing the pinhole collimator and the detector, a mouse as the object, and the imaging desk. The wide arrow depicts the rotation path of the collimator/detector set for data acquisition. (b) The double knife-edge structure of the pinhole collimator. (c) Tilt angle of the collimator/detector set.

the user's perspective is a desk having a specified position for laying the object or the animal model on it. The head rotates around the normal axis of the desk maintaining its tilt angle to acquire projection data in various views in a step-and-shoot way. In each view, similar to all pinhole-collimator-based systems, the activity distribution of a conical volume of the space is sampled and projected onto the detector forming projection data. Obviously, the apex of the cone is the pinhole; the cone axis is tilted equal to the tilt angle of the detector/collimator set. The tomographic FOV will be defined by the overlap of all such conical volumes sampled in different views and will be reconstructed via an appropriate iterative image reconstruction algorithm. During data acquisition, the object to be scanned is placed on the stationary desk. The material of that part of the desk, which is dedicated to placing the object, should be as transparent as possible to gamma rays, mainly carbon fiber.

In the current phase of the work, dedicated mainly to evaluation and performance assessment of the proposed system, we used pinhole collimation together with a monolithic scintillator crystal as the detection system. Based on the thorough comparisons and findings of Bom *et al.*,[38] regarding the effects of different materials for pinhole collimation, we used tungsten for the collimator. The thickness of the collimator is 5 mm leading to attenuation of unattended photons in the order of 10^{-8}. The characteristics of the scintillator detector we applied are summarized in Table I. Since one of our priorities was to reach submillimeter spatial resolution, besides acceptable sensitivity, the physical parameters were set to enable an appropriate zoom factor. The pinhole was designed with a double knife-edge shape with 1 mm diameter [Fig. 1(b)]. Correspondingly, pinhole-to-center-of-image-matrix distance (*po*), pinhole-to-detector distance (*pd*), and pinhole knife-edge opening angle were 18.75 mm, 300 mm,

TABLE I. The characteristics of the scintillator detector used for the SPECT system.

Material	NaI(Tl)
Dimensions	30 cm×30 cm×3/8 in.
Energy resolution	10% at 140 keV
Intrinsic spatial resolution	3 mm
Energy window	125–155 keV
Projection matrix size	512×512

and ~56°, respectively. For all scans reported in this work, the abovementioned values were utilized, except if stated otherwise.

2.B. Image reconstruction algorithm: Finite-aperture-based circular projections (FABCP)
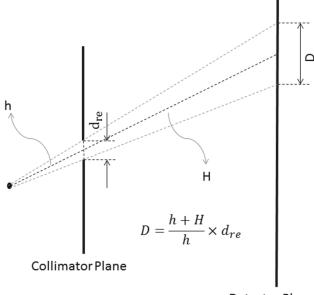
Regarding the unusual geometry of the PERSPECT, an iterative image reconstruction algorithm based on maximum-likelihood expectation–maximization (MLEM)[47,48] was developed. A model of the system needed to be used through back-projection and forward projection in each subiteration of the reconstruction algorithm. The more accurate the model for the projector–backprojector pair, the better the resultant reconstructed images. As a highlight, instead of considering an ideal pinhole in the algorithm, we assumed a finite-aperture pinhole. In addition, we used the effective diameter instead of the physical diameter of the pinhole to take into account the penetration through the collimator. However, instead of using the effective diameter for sensitivity (d_e), which has been basically defined for sensitivity calculations (see Sec. 2.C.2 for more details about the effective diameter for sensitivity), the effective diameter for resolution (d_{re}) was applied, defined as the diameter of a pinhole without penetration, giving a resolution equal to the pinhole including penetration, as given by[49,50]

$$d_{re} = d \times \left(1 - \ln(0.5) \times \frac{\tan\left(\frac{\alpha}{2}\right)}{\mu \times d} \right). \qquad (1)$$

From the pinhole collimator parameters, d_{re} was calculated as 1.03 mm. Then, instead of a knife-edge pinhole collimator of tungsten, we considered an ideal planar collimator with a circular pinhole with diameter of d_{re}.

The algorithm starts with an initial estimate for the image. A simple estimate (all voxels set to "one") is used. The framework is essentially a subsetized approach to image reconstruction,[51] since after every view, a new image estimate is created (given 16 views, this corresponds to 16 subsets/iteration).

As shown in Fig. 2, the photons emitted isotropically from each voxel form a cone passing the pinhole. The forward projection step finds the cross section of the cone with the detector plane, distributing each image voxel value to the detector bins corresponding to the cross section, and finally

FIG. 2. The projection of a typical image voxel passing through the pinhole is a circle when the collimator and the detector planes are parallel. The position of the center of the circle and its diameter can be analytically calculated. H, h, d_{re}, and D denote distance from the center of the pinhole to the center of the circle, distance from the voxel to the center of the pinhole, resolution-related effective diameter of the pinhole, and the diameter of the circle, respectively.

calculating the superposition of the impact of all image voxels on the detector. With respect to the circular shape of the pinhole, and the fact that the collimator plane and the detector plane are parallel to each other, it can be shown that the cross section of a given cone whose apex is one of the image voxels passing through the pinhole is a circle on the detector plane. The location of the circle on the detector plane as well as its diameter can be analytically obtained (Fig. 2). The value of the image voxel is then distributed between the projection bins inside the circle. The backprojection process is performed similarly in a reverse process.

We called the image reconstruction algorithm *FABCP*, given the method of modeling the pinhole in the projector–backprojector pair. This approach is a subset of collimator–detector response function (CDRF) modeling methods, as we elaborate in the Discussion section.

2.C. Monte Carlo simulations

2.C.1. GATE

GATE is a toolkit for MC simulation in nuclear medicine, CT, and internal dosimetry. It is based on reliable libraries of Geant4 providing a modular and versatile tool for various applications, e.g., modeling, design, optimization, and so on.[44,45,52] In this work, we applied GATE 6.1 for MC modeling of the proposed PERSPECT system. The ability of GATE in modeling uncommon geometries and movements was particularly advantageous in the current study. Besides, the capability of simulating a wide range of sources including ideal (dimensionless) point sources was favorable.

2.C.2. Sensitivity

The sensitivity of a pinhole collimator along its axis is given by[38,49,53–57]

$$S = \frac{d_e{}^2}{16h^2}, \tag{2}$$

where h is the distance of the source from the pinhole and d_e denotes the effective diameter of the given pinhole, which is defined as the diameter of a pinhole without penetration that would have matched sensitivity, and is given by

$$d_e = \left(d \times \left(d + \frac{2}{\mu} \times \tan\left(\frac{\alpha}{2}\right) \right) \right)^{1/2}, \tag{3}$$

where d, μ, and α denote the physical diameter of the pinhole, linear attenuation coefficient of the collimator, and the opening angle of the pinhole, respectively.

In order to evaluate the sensitivity of the system and then compare it with the theoretical value obtained for the pinhole collimator, an ideal point source with an activity of 3.7 MBq (100 μCi) of Tc-99m was placed at the center of the image matrix (at distance of 18.75 mm from the pinhole) and a 960 s scan was simulated. The sensitivity was then calculated as the total detected events divided by the total emitted photons (or divided by time) for showing the sensitivity in terms of fraction (or in terms of cps/MBq).

2.C.3. Image quality against tilt angle

As described earlier, one basis for the system concept is the tilt of the head. The tilt angle is shown in Fig. 1(c). We performed a set of simulations to assess spatial resolution, contrast, noise, uniformity, and normalized squared error (NSE) (as a measure of similarity between the resultant image and the reference image) with changes in the tilt angle. Given the fact that the detector/collimator set is located underneath the scanning desk, there is a lower limit for the tilt angle. Based on the sizes of the detector and the collimator assumed, the lower limit for tilt angle was calculated at about 30°. The theoretical higher limit for it is obviously 90°, though using 90° tilt leads to similar projection data in different views and hence is not appropriate for image reconstruction.

To calculate spatial resolution, a set of 6 Tc-99m point sources were placed at different locations in the FOV and scanned in 16 views over 360° span using MC simulation. Supposing that the center of the 3D image matrix is at Cartesian coordinates (0, 0, 0 mm), the positions of the six point sources are stated in Table II. Such a configuration was set to obtain the spatial resolution in various positions in the FOV. Scans were repeated with changes in the tilt angle from 0° to 75° with steps of 15°. Although tilt angles lower than 30° cannot be implemented in the current configuration (as explained earlier), given the main concept of the design, they were assessed to provide a better picture of the behavior of the system with changing the tilt angle. The tilt angle of 0° is in fact equivalent to a conventional single-pinhole collimator SPECT imaging.

Sources	Cartesian coordinates (in mm)
Source #1	$(0,-5,-5)$
Source #2	$(0,0,-5)$
Source #3	$(0,-5,0)$
Source #4	$(0,0,0)$
Source #5	$(0,-5,5)$
Source #6	$(0,0,5)$

Images were then reconstructed by three iterations using image voxel size of $(0.2 \text{ mm})^3$. In the reconstructed images, the full-width at half-maximum (FWHM) of the Gaussian fitted on the count profile of each point source in three dimensions was calculated. Consequently, 18 values were obtained for spatial resolution of the six sources in three dimensions. Also, for each tilt angle, the mean spatial resolution and the percentage coefficient of variation (%CV) along each dimension were calculated as well as the overall spatial resolution and %CV (i.e., averaged along all 3 dimensions and 6 points sources).

Moreover, a sphere with diameter of 10 mm centered in the image matrix with uniform activity concentration of Tc-99m (total activity of 2.8 mCi) was simulated and scanned in 16 views over a 360° span with different tilt angles (the same as before) to be used for calculating NSE, noise [in terms of percentage standard deviation (STD%)], and uniformity. Images were then reconstructed by three iterations using image voxel size of $(0.2 \text{ mm})^3$. For calculating NSE, the resultant image was normalized to the mean value of the 3D image and compared with the reference image, which is a 10 mm-diameter sphere in a matrix with the same size as the matrix of the resultant image normalized to the mean value of the 3D matrix

$$\text{NSE} = \frac{\sum_{n=1}^{N} (I(n) - I_{\text{ref}}(n))^2}{\sum_{n=1}^{N} (I_{\text{ref}}(n))^2}, \tag{4}$$

where I, I_{ref}, n, and N denote the reconstructed image matrix, the reference image matrix, the voxel index number, and the total number of voxels in the matrix, respectively.

Using the same image, uniformity was calculated on a volume of interest (VOI) drawn as a sphere concentric with the reference sphere though with diameter of 7.5 mm. STD% was additionally computed for the selected VOI. Another metric was the following:

$$\text{non\_uniformity}(\%) = 100 \times \frac{\text{max} - \text{min}}{\text{max} + \text{min}}, \tag{5}$$

where *max* and *min* are the maximum and the minimum values in the VOI.

In order to measure the contrast, a sphere with diameter of 10 mm (as background region) including a concentric sphere with diameter of 3 mm (as hot region) was used. Both spheres had uniform activity of Tc-99m; the activity concentration of the hot region was about 4.7 times the one of the background

region. Contrast was calculated as follows:

$$\text{Contrast} = \frac{mean_H/mean_{BG} - 1}{A_H/A_{\text{BG}} - 1}, \tag{6}$$

where $mean_H$ and $mean_{BG}$ denote the mean values of the hot and the background regions, respectively, and A_H/A_{BG} is the actual concentration ratio between the hot and the background regions.

2.C.4. Image quality against number of iterations

To find out the effect of the number of iterations in image reconstruction on the quality of the resultant images, a similar procedure as utilized for measuring NSE, noise, uniformity, and contrast in Sec. 2.C.3 was applied with tilt angle of 30°. However, for spatial resolution calculations, a single point source at the center of the image matrix was simulated. Data were then reconstructed using different numbers of iterations, and subsequently, NSE, noise (STD%), uniformity, contrast, and spatial resolution were calculated similarly to the methods described in Sec. 2.C.3. Moreover, contrast-to-noise ratio (CNR) was calculated as follows:

$$\text{CNR} = \frac{mean_H - mean_{BG}}{\sigma_{\text{BG}}}, \tag{7}$$

in which σ_{BG} is the standard deviation of the background region.

2.C.5. Contrast-to-noise ratio against size of hot-region

To quantify the probable effect of hot region size on the corresponding measured CNR, a set of simulations the same as the setup for contrast simulations in Sec. 2.C.3 was performed. The simulation was repeated with spherical hot regions with diameters of 1, 3, and 5 mm, while a spherical background region with 10 mm diameter surrounded them. For all simulations, concentration ratio between the hot and the background regions was 4.7. All data sets were reconstructed with voxel size of $(0.2 \text{ mm})^3$ by three iterations.

2.C.6. System FOV

Given the new geometry and data acquisition protocol for the PERSPECT, the FOV cannot be determined in a straightforward manner. Taking into account that the FOV is the portion of spatial volume imaged by all views, in order to determine the potential FOV, all voxels of the image matrix are assessed using an in-house code to check if they are sampled by all views or not. Those voxels fulfilling that criterion contribute to the potential FOV of the system. The overall FOV of the system is the portion of the potential FOV, which can be reconstructed having enough number of view numbers and enough difference between the acquired projection data of the views.

2.D. The analytical simulator

The purpose of imaging with a gamma camera is to depict the distribution of a radionuclide within a patient or animal body after its administration. This needs a detector around the body to record the gamma rays as emitted from the radionuclides, passed through body, and having interacted with the detectors. The process of image formation can be mathematically described as a continuous integral model.

The procedure of image formation in a gamma camera made of scintillator crystals coupled to PMTs can be concisely depicted as the diagram in Fig. 3. With respect to the diagram, considering the object as a voxelized matrix and discretized projection bins, and using the voxel-driven method,[41,58] the image formation process can be analytically modeled.

The first step for simulating the scan process of an object in our simulator is defining the activity distribution as a 3D voxelized source matrix. The voxelized source can be generated with any desired method including the application of digital phantoms such as 4D MOBY phantom.[46] Smaller voxel sizes lead to a more accurate object modeling due to emulation of a condition more similar to the reality with theoretical voxel size value of zero. Since the degrading effects of attenuation in small-animal imaging are much less than in clinical imaging,

and this effect is more remarkable in rat-size imaging or for accurate quantitative imaging purposes,[59] we have not considered attenuation in the analytical simulator for ease of implementation and higher speed. Also, Compton scattering was not considered in the analytical simulator. Forward projection process then starts by projecting each voxel to the detector taking into account the pinhole collimator. For speeding up the algorithm, no voxels in the object are discarded. The forward projection is performed the same as what is used in FABCP forward-projector module. In order to model the collimator including its edge penetration effects, the tungsten knife-edge aperture is modeled by a circular aperture in a plane with infinite attenuation. Effective diameter for resolution (d_{re}), as defined and formulated earlier, is considered as the diameter of the circular aperture.

Supposing that the voxels in the object matrix are determined small enough, the projection of each voxel on the detector passing through the circular pinhole would be a circle. The location and diameter of the corresponding projection circle can be analytically calculated as in FABCP. The value of the object voxel then is distributed to the bins surrounded by the projection circle. Besides, scan time of each view is modeled by multiplying the value of each voxel by the corresponding scan time prior to distributing the value to the
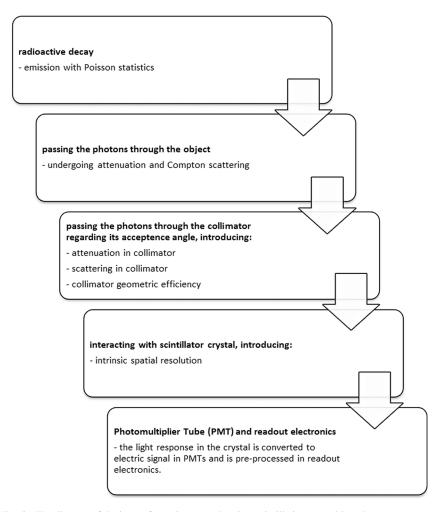

Fig. 3. The diagram of the image formation procedure in a scintillation-crystal-based gamma camera.

related projection bins. It should be remarked that geometric efficiency (sensitivity) of the pinhole collimator is also modeled by multiplying each voxel value by its corresponding location-dependent geometric efficiency value (considering its relative location to the pinhole in each projection view) prior to distributing its value to the corresponding projection bins in the detector. The geometric efficiency, E, for each voxel is calculated by[60]

$$E = \frac{d_e{}^2 \times \sin\theta^3}{16 \times h^2}, \tag{8}$$

where θ is the incidence angle of the hypothetical line connecting the voxel to the center of the aperture on the aperture plane. The effective diameter is calculated as in Eq. (3).

Finally, the superposition of the projections of the all voxels gives the projection matrix corresponding to the whole voxelized source matrix for the predetermined projection view. The same procedure should be performed for each view knowing that the positions of the pinhole aperture and the detector change with respect to the view angle.

The intrinsic spatial resolution of the detector is also modeled in the analytical simulator. For this, a digital 2D Gaussian function is generated using a chosen value for the detector intrinsic spatial resolution. Convolving each projection view by the 2D Gaussian function emulates the effect of the intrinsic spatial resolution.

The statistical noise is also modeled by considering Poisson statistics for the projection matrix obtained from the previous step. It is noted that instead of adding artificial noise to the data, Poisson noise is generated using the projection matrix values.

Although the simulator was developed for modeling the PERSPECT, its code was implemented in a generic way so that not only any parameter of the system can be modified conveniently but the code can also be applied for simulating other conventional pinhole systems (by assuming a tilt angle of 0°). Generating the preferred number of projection views, one can then reconstruct the acquired data using the FABCP image reconstruction algorithm.

2.D.1. Evaluation of the analytical simulator

In this section, a set of simulations were performed by the analytical and GATE MC simulators with the same setup to compare the results of the analytical simulator with the MC simulation results.

Three sets of simulations were performed: (i) ideal point source, (ii) a 5 mm-radius sphere with uniform activity, and (iii) a 1.5 mm-radius sphere with uniform activity. The same setup for the system was used for both types of simulations including pinhole-to-the-center-of-the-image-matrix distance, pinhole-to-the-detector distance, tilt angle, detector size, and pinhole physical diameter of 18.75 mm, 300 mm, 30°, 300 mm, and 1 mm, respectively. No attenuation or scattering was simulated for the phantoms.

First, an ideal point source (dimensionless in GATE and 1×10^{-18} m in the analytical simulator) with activity of 740 kBq was simulated at the center of the FOV. Data acquisition was performed in 16 views (60 s per view) through 360° span.

Projection data of both MC and the analytical simulator were stored in 512×512 matrices. Pearson correlation coefficient (R) and NSE were computed for MC and the analytical simulator data as similarity measures. R-values of each two corresponding projection data in MC and the analytical simulator data sets were averaged to form $R_{P,\text{ mean}}$.

Similarly, mean NSE ($\text{NSE}_{P,\text{ mean}}$) was calculated as the average of the NSE values of each two corresponding projection data in MC and the analytical simulator data sets. Each matrix was normalized to its mean value before NSE computation. NSE was calculated using Eq. (4) considering the MC data as the reference.

Both MC and the analytical simulator data were then reconstructed using FABCP algorithm. The image reconstruction was performed using image voxel size of $(0.2 \text{ mm})^3$ and three iterations. Similar to the processes performed for the projections, the similarity between the reconstructed images (in the form of 3D matrices) from the analytical simulator and MC data was assessed in terms of the Pearson correlation coefficient (R_I) and NSE_I. Prior to NSE calculation, each image data set was normalized to its mean value.

Moreover, a sphere of 5 mm radius, located at the center of the FOV, with uniform activity concentration (total activity of 104 MBq) was simulated by both MC and the analytical simulator. Data acquisition was performed in 16 views (60 s per view) through 360° span. The projection data were stored in 512×512 matrices. The same as the method described in the point source simulation, $R_{P,\text{ mean}}$ and $\text{NSE}_{P,\text{ mean}}$ were calculated. The projection data of MC and the analytical simulator were then reconstructed using the FABCP image reconstruction algorithm by three iterations and voxel size of $(0.2 \text{ mm})^3$. The reconstructed images were used to compute R_I and NSE_I.

In addition, another simulation, similar to the previous one, was performed but with a 1.5 mm-radius sphere at the center of the FOV with uniform activity concentration (total activity of 10 MBq). $R_{P,\text{ mean}}$, $\text{NSE}_{P,\text{ mean}}$, R_I, and NSE_I were then calculated.

2.D.2. Simulation of the micro-Derenzo phantom

Two micro-Derenzo phantoms with different hole sizes but with the same structure were defined to assess the quality of the reconstructed images of the system, especially the spatial resolution of the system more realistically. Both phantoms consist of six sections of hot rods. The phantoms were defined using an in-house code in $201 \times 201 \times 201$ matrices with voxel size of $(0.1 \text{ mm})^3$ and $(0.05 \text{ mm})^3$ for the larger and the smaller phantoms, respectively. More details of the phantoms are summarized in Table III.

In the first simulation, *po, pd*, tilt angle, detector size, and pinhole physical diameter of 18.75 mm, 300 mm, 40°, 500 mm, and 0.5 mm were considered, respectively. The larger micro-Derenzo phantom was used for this setup. The phantom was simulated such that the rods were perpendicular to the imaging desk. Data acquisition was performed in 16 views (120 s per view) over 360° scan. Data were then reconstructed using $(0.2 \text{ mm})^3$ voxel size and three iterations by the FABCP image reconstruction algorithm.

TABLE III. The detailed specifications of the defined micro-Derenzo phantoms.

	The larger micro-Derenzo	The smaller micro-Derenzo
Diameter (mm)	20	10
Thickness (mm)	20	10
Total activity (MBq)	74	74
Section sizes:		
	4.9 mm	2.4 mm
	4.2 mm	2.1 mm
	3.3 mm	1.6 mm
	2.5 mm	1.2 mm
	1.7 mm	0.8 mm
	1.2 mm	0.6 mm

In the second set of simulations, the smaller micro-Derenzo phantom was used. The same data acquisition and system parameters were applied, while the pinhole physical diameter was set to 0.25 mm to assess the effect of smaller aperture size on spatial resolution. In addition, two independent simulations were performed. Once, the phantom was placed in a way the rods were perpendicular to the imaging desk and then in a way they were parallel to the imaging desk. Both sets of data were reconstructed using $(0.1 \text{ mm})^3$ voxel size and three iterations by FABCP algorithm.

2.D.3. Simulation of the pseudo-Defrise phantom

Although it is known that pinhole collimators have an inherent weakness in imaging the Defrise phantoms due to incomplete sampling (along the axial direction in conventional SPECT imaging), we simulated a pseudo-Defrise phantom, once with disks oriented parallel to the imaging desk and then perpendicular to it to show such an effect. The phantom contained 10 disks (10 mm in diameter and 1 mm thick) with uniform activity of 200 MBq for each disk. Scan parameters of *po, pd,* tilt angle, detector size, and pinhole physical diameter of 18.75 mm, 300 mm, 30°, 500 mm, and 0.25 mm were considered, respectively. Data acquisition was performed in 16 views (120 s per view) over 360° scan. Data were then reconstructed using $(0.2 \text{ mm})^3$ voxel size and three iterations by FABCP image reconstruction algorithm.

2.D.4. Simulation of the MOBY phantom

Since the PERSPECT is going to be used for small-animal imaging, 4D MOBY digital phantom[46] was applied to assess the ability of the system in imaging of a digital mouse phantom using the analytical simulation. For this, the activity distribution in a mouse with body height, body long axis, and body short axis of, respectively, 91, 26.7, and 25 mm was generated in a 3D matrix with voxel size of $(0.1 \text{ mm})^3$. Two separate scans were performed simulating a cardiac scan and a renal scan. For each scan, the object was laid on the imaging desk in a way the center of the organ of the interest (the heart in the cardiac scan and the kidneys in the renal scan) was almost

in the center of the FOV. Total activity of 148 and 74 MBq was considered to be administered to the mouse for the cardiac scan and the renal scan, respectively. For both simulations, *po, pd,* tilt angle, detector size, and pinhole physical diameter of 18.75 mm, 300 mm, 40°, 500 mm, and 0.5 mm were considered, respectively. Data acquisition was performed in 16 views (120 s per view) over 360° span. Projection data in each view were stored in a 512×512 matrix.

Regarding the small FOV of the system in comparison to the size of the MOBY phantom (the mouse), not whole body of the mouse can be scanned and reconstructed in a single bed position. However, reconstructing a part of the MOBY phantom in a small image reconstruction matrix may affect the quality of the resultant images due to the effects of the truncation occurs in most of projection views. To testify a compensation method for such effects, data were reconstructed using two image matrix sizes: a matrix approximately with the size of the potential FOV [small matrix: $151 \times 101 \times 151$, voxel size of $(0.2 \text{ mm})^3$] and a matrix approximately with the size of the MOBY phantom [large matrix: $151 \times 601 \times 151$, voxel size of $(0.2 \text{ mm})^3$]. FABCP algorithm with three iterations was applied.

3. RESULTS

3.A. Monte Carlo simulations

3.A.1. Sensitivity

The effective pinhole diameter as given by Eq. (3) is 1.14 mm. The sensitivity was analytically calculated as 0.023%. The sensitivity as calculated using MC simulations was 0.021% (207 cps/MBq).

3.A.2. Image quality against tilt angle

Figure 4(a) shows that the NSE has no major variation until tilt angle of 45°. From tilt angle of 45°, NSE begins a fast increase. Contrast shows a very moderate decrease up to 75° tilt angle. At that tilt angle, contrast decreases substantially. Uniformity and STD% are shown together in Fig. 4(b) for the selected VOI. In addition, Fig. 4(c) shows mean spatial resolution along each dimension together with the overall mean spatial resolution, i.e., overall dimensions as obtained for the set of six point sources (as described in earlier sections). It is noticeable that with increasing tilt angles, the spatial resolution along the *z* direction (i.e., perpendicular to the imaging desk) degrades the most, which is expected. However, what is noteworthy is that this only occurs for tilt angles exceeding 45° and especially 60°. As such, this favorably demonstrates that our proposed approach to open-gantry desktop imaging at ∼30° is viable.

Figure 4(d) illustrates the spatial resolution variation along each dimension and overall variation of the values in terms of CV% for different values of tilt angle. According to the acquired results and the lower physical limit for the tilt angle, 30° was selected for the tilt angle.

Figures 5(a)–5(e) depict a sample slice of the reconstructed image showing two of the point sources, a sample slice of

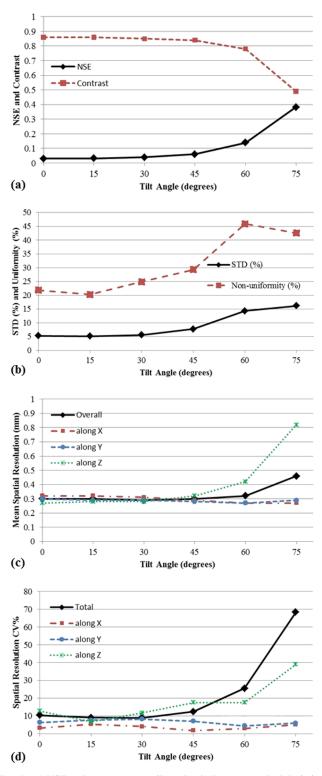**(a)**

(b)

(c)

(d)

FIG. 4. (a) NSE and contrast versus tilt angle. (b) Percent standard deviation and nonuniformity versus tilt angle measured using a 10 mm-diameter sphere with uniform activity. (c) Spatial resolutions (in terms of FWHM) versus tilt angle measured using a set of six ideal point sources at different positions in the FOV. (d) CV% of spatial resolution for the mentioned set of point sources.

the reconstructed image of the sphere with uniform activity, 3D-rendered maximum intensity projection (MIP) image of the point sources, 3D-rendered MIP image of the sphere, and a sample slice of the reconstructed image of the
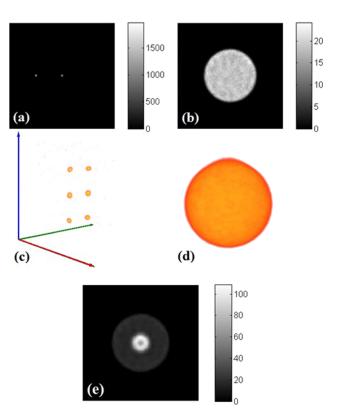

FIG. 5. (a) and (b) Sample slices of the reconstructed images of the set of point sources and sphere with uniform activity, respectively. (c) and (d) 3D-rendered MIP images of the point sources and the sphere, respectively. (e) The middle slice of the reconstructed image of the contrast phantom. Data acquisition was performed at 30° tilt angle and data were reconstructed using three iterations. The red, green, and blue axes in (c) denote, respectively, x, y, and z axes. The slices shown in (a), (b), and (e) are parallel to x–y plane. (See color online version.)

contrast phantom at a tilt angle of 30° reconstructed by 3 iterations.

3.A.3. Image quality against number of iterations

Figures 6(a)–6(f) show NSE, uniformity, noise (in terms of STD%), contrast, CNR, and spatial resolution, respectively. As seen in Fig. 6(a), using the described phantoms, the minimum value of NSE happens at the 4th iteration, although showing no substantial difference with the value obtained at 3rd iterations. Based on Fig. 6(b), the resultant image has the most uniform state at the third iteration while worsening with increasing the number of iterations. According to Figs. 6(c)–6(e), the lowest value of noise occurs at the third iteration while neglecting the second iteration, contrast has almost a flat trend with increasing the number of iterations. Hence, CNR maximum value happens at the 3rd iteration. As shown in Fig. 6(f), spatial resolution has generally no remarkable variation after the second iteration.

3.A.4. Contrast-to-noise ratio against size of hot-region

CNR was calculated using Eq. (7) as 26.3, 14.7, and 10.7 for hot region diameter of 1, 3, and 5 mm, respectively. The
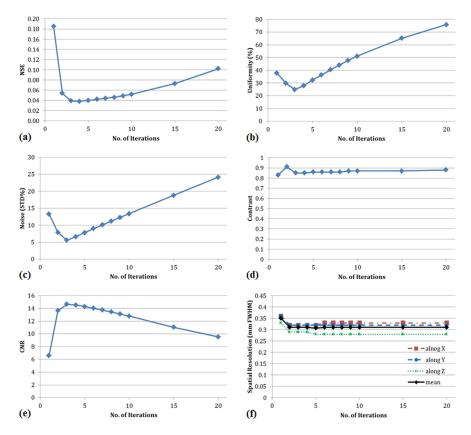
FIG. 6. (a) NSE versus number of iterations. (b) Uniformity versus number of iterations. (c) Noise [in terms of percent standard deviation (STD%)]. (d) Contrast versus number of iterations. (e) CNR versus number of iterations. (f) Spatial resolution (in terms of FWHM) of a point source along each axis together with the mean of spatial resolution values along all three axes versus number of iterations. For these studies, a point source in the center of the FOV was utilized.

results showed that a better CNR value is obtained when the hot region is smaller.

3.A.5. System field-of-view

Figures 7(a)–7(g) show the 3D-rendered MIP image of the system potential FOV (as described earlier) at tilt angles of 0°–90° in a $101 \times 101 \times 101$ matrix with voxel size of $(0.2 \text{ mm})^3$. As expected, the FOV at tilt angle of 0° is the same as the FOV of a pinhole SPECT system with a conventional movement. With increasing the tilt angle, the potential FOV gets larger. But, as it will be described in Discussion, this does not necessarily result in a larger FOV, which is able to be reconstructed.

3.B. Analytical simulations

3.B.1. Evaluation of the analytical simulator

The first projection view (as a sample view) of the point source and the spherical uniform phantoms with radii of 5

and 1.5 mm are shown in left, middle, and right column of Fig. 8. The top row illustrates the projections obtained by the MC simulation, while the bottom row corresponds to the projections resulted from the analytical simulation. As shown, the projections of the MC and the analytical simulations are qualitatively similar.

The obtained values for $R_{P, \text{mean}}$ and $\text{NSE}_{P,\text{mean}}$ for the three phantoms (the point source and the two spherical sources) are summarized in Table IV. In addition, STD of R-values (Pearson correlation) between each two corresponding projection data obtained using MC and analytical methods and the NSE values of each two corresponding projection data in MC and the analytical simulator data sets were also reported as STD of R_P and STD of NSE_P, respectively, to show the dispersion of the data. The quantitative results show that the correlation of the analytical simulator projections with corresponding MC projections is in an acceptable range. Also, mean NSE of the analytical simulator projections and the MC projections has small values for all three types of phantoms.
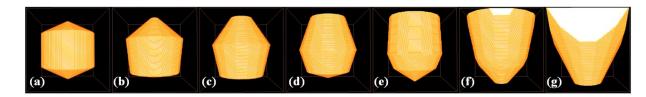

FIG. 7. [(a)–(g)] 3D-rendered MIP image of the system potential FOV at tilt angle of 0°, 15°, 30°, 45°, 60°, 75°, and 90° bounded in a $(20 \text{ mm})^3$ image matrix.
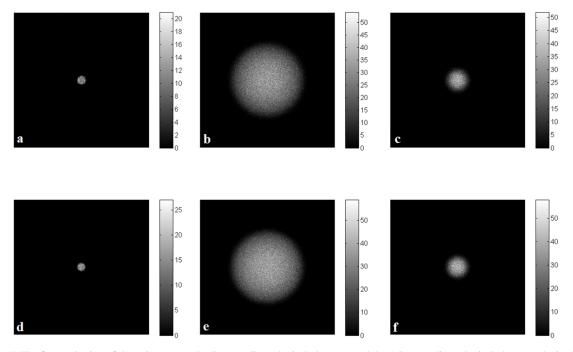
FIG. 8. [(a)–(c)] The first projection of the point source, the 5 mm-radius spherical phantom, and the 1.5 mm-radius spherical phantom obtained by the MC simulation, and [(d)–(f)] the first projection of the point source, the 5 mm-radius spherical phantom, and the 1.5 mm-radius spherical phantom obtained by the analytical simulation.

The central slices (parallel to the imaging desk plane) of the reconstructed images of the three phantoms are shown in Fig. 9. The top row corresponds to the images reconstructed from the MC data and the middle row images were reconstructed from the analytical simulator data. The bottom row depicts the count profile of the central row of the sample slices. As shown in Fig. 9, the reconstructed images of all three phantoms are almost the same for the MC and the analytical simulation data.

To quantitatively compare the reconstructed images from the MC data and the analytical simulator data, R_I and NSE_I were calculated for each set of the images as described in Sec. 2.D.1. The obtained results were summarized in Table V. The results reflect the similarity of the reconstructed images from the MC and the analytical simulator. Moreover, for assessing the accuracy of geometric efficiency modeling in the reconstruction algorithm, total activity of each reconstructed data set was calculated as sum of the 3D image matrix normalized to the time per view of the corresponding scan.

3.B.2. Simulation of micro-Derenzo phantom

Figures 10(b)–10(d) show sample slices of the reconstructed images of the larger micro-Derenzo phantom perpendicular to the imaging desk with 0.5 mm aperture, the smaller micro-Derenzo phantom parallel to the imaging desk with 0.25 mm aperture, and the smaller micro-Derenzo phantom perpendicular to the imaging desk with 0.25 mm aperture, respectively. A sample slice of the used micro-Derenzo phantom is also shown in Fig. 10(a) as a reference for comparison. Except for the sample slice in Fig. 10(c), which is perpendicular to the imaging desk plane, the other slices in Fig. 10 are parallel to the imaging desk. The images were normalized to the maximum value in the slice for better illustration. As shown in Fig. 10(b), using 0.5 mm diameter aperture and the larger phantom, all sections were resolved including the smallest section (1.2 mm). However, using 0.25 mm and the smaller phantom, the smallest section (0.6 mm) was not resolved as good as the other sections though still most of its rods can be considered as resolved.

3.B.3. Simulation of the pseudo-Defrise phantom

Figures 11(a) and 11(c) show the central slice of the reconstructed image of the pseudo-Defrise phantoms parallel and perpendicular to the imaging desk, respectively. In addition, the count profiles of the slices are plotted in Figs. 11(b) and 11(d) after a summation along the disk orientations.

3.B.4. Simulation of the MOBY phantom

Figure 12(b) shows a sample transaxial slice of the reconstructed image of the MOBY phantom in cardiac scan using
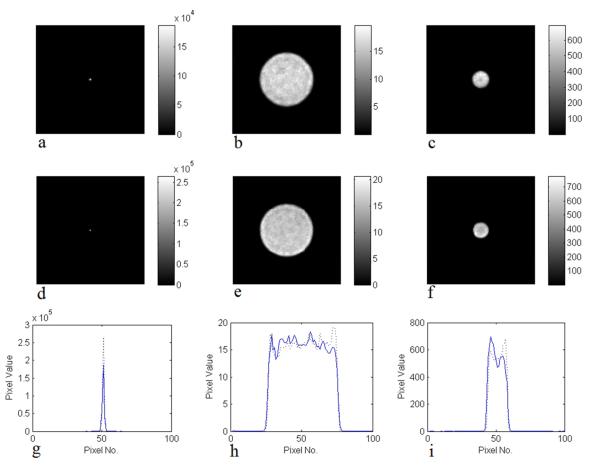
TABLE IV. Mean and standard deviation of R-values of each two corresponding projection data in the MC and the analytical simulator data sets, R-values of the MC projection views, and the NSE values of each two corresponding projection data in the MC and the analytical simulator data sets.

	Point source	Sphere (5-mm radius)	Sphere (1.5-mm radius)
$R_{P,\,mean}$	0.89	0.95	0.96
STD of R_P	0.0039	0.0004	0.0014
$NSE_{P,\,mean}$	0.26	0.08	0.08
STD of NSE_P	0.0121	0.0008	0.0028

FIG. 9. [(a)–(c)] The central slices of the images of the point source, the 5 mm-radius sphere, and the 1.5 mm-radius sphere reconstructed from the MC simulation data, [(d)–(f)] the central slices of the images of the point source, the 5 mm-radius sphere, and the 1.5 mm-radius sphere reconstructed from the analytical simulation data, and [(g)–(i)] the count profiles of the central row in the central slices of the reconstructed images of the point source, the 5 mm-radius sphere, and the 1.5 mm-radius sphere; the solid line corresponds to the MC data and the dashed line corresponds to the analytical simulator data. The images (hence the count profiles) were normalized to mean value of the corresponding 3D reconstructed images.

the small reconstruction matrix. Figure 12(c) demonstrates the same slice while the large reconstruction matrix was used. The same slice in the modeled voxelized phantom is also shown in Fig. 12(a) as a reference. Similarly, Figs. 12(e) and 12(f) show the same sample slice of the reconstructed image of the MOBY phantom in coronal direction in renal scan using the small and the large image reconstruction matrixes, respectively. Figure 12(d) shows the same slice in the modeled voxelized phantom. The reference slices [(a) and (d)] were normalized to the slice maximum value.

4. DISCUSSION

A new concept for SPECT imaging was proposed primarily based on a tilted collimator/detector pair located beneath the scanning desk. In other words, the system does not have a closed-gantry configuration. Instead, it is replaced with a so-called imaging desk that has a determined region for placement and scanning. Using such a system has a number of advantages. Having a desk instead of a closed-gantry configuration provides users with ease in handling of small animal. Any kind of monitoring, attaching gating facilities, utilizing anesthesia apparatus, etc. are made more feasible while the

animal is laid on a desk. Furthermore, this approach enables potentially easier tracking of motion for awake animal imaging, which is restricted in closed-gantry setups.[27–29] In the PERSPECT prototype, a micro CT can also be implemented to provide anatomical data together with attenuation correction possibility. However, adding an X-ray tube and CT detector to the system alters the completely open configuration of it

TABLE V. Correlation coefficient (R_I) and NSE (NSE$_I$) of each two corresponding reconstructed images from the MC and the analytical simulator data sets together with the total activity value simulated and the value obtained after reconstruction and normalizing by time per view of the corresponding scan.

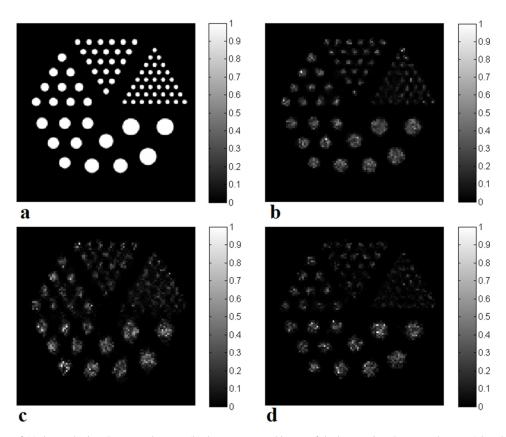|		Point source	Sphere (5-mm radius)	Sphere (1.5-mm radius)
	R_I	0.95	0.99	0.98
	NSE$_I$	0.50	0.01	0.04
Total activity	Simulated	740.0 kBq	104.0 MBq	10.0 MBq
	Reconstructed from MC	680.6 kBq	90.3 MBq	9.2 MBq
	Reconstructed from analytical simulator	747.2 kBq	104.8 MBq	10.4 MBq

FIG. 10. Sample slices of (a) the used micro-Derenzo phantom, (b) the reconstructed image of the larger micro-Derenzo phantom (placed perpendicular to the imaging desk) using 0.5 mm aperture, (c) the reconstructed image of the smaller micro-Derenzo phantom (placed parallel to the imaging desk) using 0.25 mm aperture, and (d) the reconstructed image of the smaller micro-Derenzo phantom (placed perpendicular to the imaging desk) using 0.25 mm aperture.

to some extent because the tube and the detector should be placed opposite to each other having the ability to rotate around the object. A circular path on the imaging desk should be considered for adding CT apparatus. But, still the system will provide an open-gantry configuration enabling access to the object/animal from the top during the SPECT or CT scan.

In addition, the pinhole collimator utilized in the current system enables higher spatial resolutions than parallel-hole collimators. Besides, since the system is intended for small-animal imaging, which has a small FOV and the collimator can get very close to the animal, the system can achieve acceptable levels of sensitivity. Moreover, the magnification provided by the pinhole collimator eliminates the need for a high-resolution detector, e.g., pixelated crystals coupled to PSPMTs. By contrast, a conventional monolithic scintillator crystal coupled to ordinary PMTs, with an intrinsic spatial resolution of about 3–4 mm with simple electronic and calibration methods, satisfies the requirement of the system while simultaneously decreasing the system cost. In fact, similar to some past efforts,[24,61–63] even a clinical SPECT head may be utilized for small-animal imaging. At the same time, the concept can be implemented using other types of collimators, e.g., parallel-hole collimators.

From the mechanical point of view, it is expected that in the prototype, the head rotation beneath the desk will be more stable in contrast to conventional gantry rotation. The latter can introduce some instability in gantry movements and positioning (leading to mispositioning of heads) due to variation

of the torque applied to it by gravity in different views. Being free from such mechanical-induced artifacts in the proposed system in comparison to conventional rotating gantries leads to simpler correction and calibration methods, and ultimately to images of higher quality. Furthermore, the fabrication and service costs of such a mechanical system with only one degree of freedom for movement are lower. It should also be noted that the FOV size can be altered by changing the distance of the head from the object by adding greater sophistication to the system mechanics. The system may for instance be applicable with some modifications for small-organ (e.g., breast) SPECT imaging in humans.

To reconstruct images of such a system, a dedicated image reconstruction algorithm was required. As described earlier, the FABCP algorithm based on the MLEM method was subsequently developed. The approach is somewhat similar to the method employed by Hsu and Huang[36] for modeling the finite aperture of pinhole collimators in SPECT image reconstruction, but with notable differences. The method of Hsu and Huang considers a line between each detector bin and image voxel pair. If the line passes through the pinhole, then the calculations regarding how the voxel value is distributed in the detector bins are followed. But in FABCP, instead of forming and checking those lines, the projection of each voxel on the detector (which is a circle) is directly formed. Hence, the FABCP code is potentially faster. Furthermore, it is potentially more accurate because deciding on whether an image voxel and a projection bin are correlated is valid only if both the
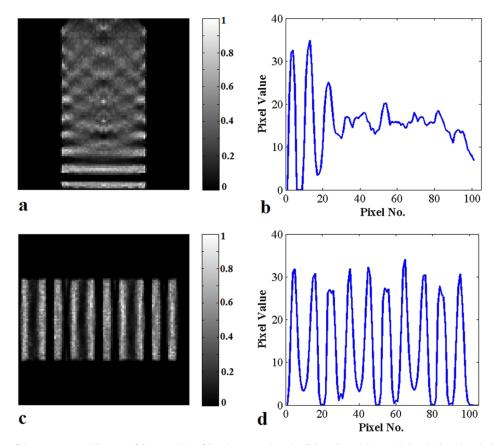
Fig. 11. Sample slices of the reconstructed images of the pseudo-Defrise phantom when the disks oriented (a) parallel to the imaging desk and (c) perpendicular to it. (b) and (d) are the count profiles of the reconstructed slices in (a) and (c), respectively, after performing a summation along disk directions.

voxel and the bin are small enough while the criterion is not always satisfied about the projection bins. At the same time, FABCP leans on the assumption of having sufficiently small voxels which is usually satisfied in high resolution systems. On the other hand, since FABCP models the finite aperture and nonideal attenuation of the collimator, it results in enhanced recovery of the resolution. The reader is encouraged to consult Refs. 64 and 65 for more details about CDRF modeling and resolution recovery in SPECT.

As earlier described in the Introduction, an exact analytical simulator was developed to be used for fast simulation of more complex phantoms. The results of the simulations performed for assessing the analytical simulator in comparison with MC simulation, summarized in Tables IV and V, demonstrate good agreement with the MC results. In addition, the real activities of the used phantoms were obtained with acceptable precision after image reconstruction that can be used for quantitative analyses.
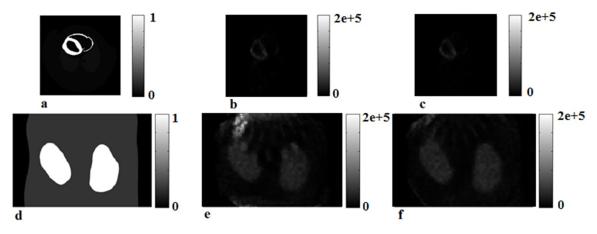

Fig. 12. The same transverse sample slices of the cardiac scan in (a) the modeled voxelized MOBY phantom, (b) the reconstructed image using the small image matrix, and (c) the reconstructed image using the large matrix. The same coronal sample slices of the renal scan in (d) the modeled voxelized MOBY phantom, (e) the reconstructed image using the small image matrix, and (f) the reconstructed image using the large matrix. (a) and (b) are normalized to the maximum value in the slice.

Since the value obtained for the sensitivity analytically only includes the collimator geometric efficiency, a real system would have lower sensitivity given the limited efficiency of the scintillator crystal and the PMTs. The sensitivity value obtained by MC simulations, as expected, was lower (by ~9%) explained by its incorporation of the intrinsic efficiency of the scintillator crystal.

In order to assess image quality performance parameters against tilt angle, a set of simulations was performed. Figure 4(a) shows that the variation of contrast with increasing the tilt angle is only minimal up to 45°. Yet, it decreases notably when the tilt angle exceeds 60°. However, it should be remarked that CNR (and contrast) as reported in Sec. 3.A.4 is sensitive to the size of hot region. But, still a single-size phantom can be used in an optimization and comparison process. Furthermore, as illustrated in the same figure, NSE has its minimum value at a tilt angle of 0° while depicting an ascending trend after it. Figure 4(b) shows the variation of uniformity and also STD% versus tilt angle. As seen, STD% as a measure of the reconstructed image noise overall increases with increasing tilt angle. Its rise is especially steep for tilt angles exceeding 30°. The uniformity of the reconstructed image also has an overall ascending trend.

The results corresponding to spatial resolution are shown in Figs. 4(c) and 4(d). As seen, the minimum value of the overall spatial resolution in three directions occurs at 30° tilt angle. Spatial resolution worsens severely with increasing tilt angle from 60° to 75°. Figure 4(c) shows that despite of uncommon data sampling of the PERSPECT along z-axis (i.e., perpendicular to the desk plane), spatial resolution along z-axis is as good as that along the other two axes before tilt angle of 60°. The variation of the spatial resolution throughout the FOV is also an important parameter measured using CV% and shown in Fig. 4(d). As shown, CV% of spatial resolution for tilt angles below 45° demonstrates an appropriate level of resolution variation through the FOV. However, it increases very fast from 45° toward 75° reaching the total value of about 68% at a tilt angle of 75°. It can be understood that the main factor of data spreading is the results along z-axis. Although, using ideal point sources can be beneficial for the aim of analyzing the behavior of spatial resolution against different factors (e.g., tilt angle), more realistic phantoms like micro-Derenzo can reflect the real spatial resolution ability of the system. As shown in Fig. 10 obtained by analytical simulations, using 0.5 mm pinhole leads to spatial resolution of 1.2 mm. Utilizing 0.25 mm pinhole results in spatial resolution of 0.6 mm.

Using the results obtained for the response of contrast, NSE, uniformity, noise (STD%), and spatial resolution to variations in tilt angle and also the practical lower limit for the tilt angle (described previously), tilt angle of 30°, which currently is in fact the minimum implementable tilt angle for the system, was considered as the default tilt angle of the PERSPECT. At a tilt angle of 30°, spatial resolution has the minimum value. Noticeably, neglecting 0° and 15° tilt angles as practically unachievable conditions, the other measured image quality parameters, i.e., contrast, noise, and uniformity would also have the optimum values.

Given the uncommon system geometry and its data acquisition protocol, estimating the tomographic FOV of the system is complex. As such, as described in the Methods section, the potential FOV was obtained for tilt angles of 0°–90°. The real FOV will be a portion of what is shown in Figs. 7(a)–7(g) that is able to be reconstructed given the number of views, etc. It is also worth noting that the FOV shape changes by varying different parameters of the system including (but not limited to) tilt angle, pinhole acceptance angle, and *po*. Meanwhile, based on Tuy condition,[66] the sampling in our system, like any other cone-beam sampling system with only one circular movement of the detector,[67] is not theoretically complete. For assessing the effects of such a sampling incompleteness, a pseudo-Defrise phantom was simulated. Although Defrise phantom is the most difficult phantom to be imaged by pinhole-based systems regarding its sharply defined planes,[68] it is used for system evaluation but its special structure is a tight constraint compared to real imaging of humans or small animals. Figure 11(a) shows that when the disks are parallel to the desk, only the first three disks are imaged well and the next disks suffer from incomplete sampling. However, for application of Defrise phantom, it is conventionally located in a manner the axis of rotation of the head(s) passes through the disks.[18] In the PERSPECT system, it corresponds to the status the disks being perpendicular to the imaging desk. In such a condition, as illustrated in Fig. 11(c) [and its corresponding count profile in Fig. 11(d)], the pseudo-Defrise phantom is reconstructed well without being degraded by incomplete sampling effects.

MOBY phantom was also simulated to assess the performance of the PERSPECT in imaging of a mouse. Figure 12 shows that the system imaged the heart demonstrating the left and right myocardia of the left and the right ventricles of the mouse and the kidneys. Meanwhile, using a large matrix in reconstruction and then cropping the matrix to a smaller one could enhance the image quality and reduce the effects of truncation, especially in the case of renal scan with the presence of a hot bladder.

The performance parameters of the system obtained within this study such as submillimeter spatial resolution, appropriate sensitivity, and FOV, in addition to easy handling and low fabrication/service cost of the system, make it favorable for application in SPECT molecular imaging. Regarding the fact that the 0° tilt angle is equivalent to a conventional single-pinhole SPECT configuration, one can compare the performance parameters of a hypothetical conventional single-pinhole SPECT with the ones of PERSPECT with different tilt angles. As shown in Fig. 4, the PERSPECT, up to tilt angle of 45°, has almost the similar values of contrast, NSE, noise (in terms of STD%), and spatial resolution in comparison with a conventional single-pinhole SPECT at the same configuration. However, uniformity of the PERSPECT is not at the similar level of a conventional single-pinhole SPECT while tilt angle in the PERSPECT increases 30°.

According to the literature, since the spatial resolution and sensitivity of small-animal SPECT systems based on pinhole/multipinhole collimators are generally more favorable compared to systems based on parallel-hole collimators, and

at the same time, the FOV of pinhole-based systems is usually smaller, comparing the PERSPECT as a pinhole-based system with parallel-hole systems is not entirely meaningful. To provide a comparison between the performance of the proposed system and that of other pinhole/multipinhole systems, we selected two high-performance small-animal SPECT systems: U-SPECT II (Ref. 22) and nanoScan.[69] Both systems utilize multipinhole collimators and multihead structure. U-SPECT II provides single-bed FOV of 12 mm × 7 mm and 27 mm × 11 mm (diameter × length) for mouse and rat imaging, respectively. The nanoScan system has three options for mouse and rat imaging including mouse organ (5 mm × 5 mm), mouse whole body/rat organ (28 mm × 12 mm), and rat whole body (56 mm × 20 mm). Although, according to Fig. 7, the FOV of the PERSPECT does not have a regular shape, it can be assumed as a cylinder with 20 mm in diameter and 20 mm in length. As such, the system FOV is larger than the mouse FOV of U-SPECT II and mouse organ FOV of nanoScan. It is nearly equivalent to rat FOV of U-SPECT II and the mouse whole body/rat organ FOV of nanoScan. Only rat whole body FOV of nanoScan is larger than the FOV of the PERSPECT. Also, it should be remarked that using a multipinhole collimator instead of a single-pinhole, one can result in a larger FOV. On the other hand, the sensitivity of U-SPECT II for Tc-99m with 1, 0.6, and 0.35 mm pinholes is 0.09%, 0.18%, and 0.07%, respectively. The sensitivity of nanoScan using basic multipinhole collimators for mouse and rat imaging was reported as 2000 cps/MBq (0.2%) and 1500 cps/MBq (0.15%), respectively. The PERSPECT sensitivity (about 0.02%) is lower than both U-SPECT II and nanoScan. The primary reason is the application of numerous pinholes in a multipinhole collimator in both systems enabling amplified detection of photons. The lower sensitivity of our system can be compensated (if needed) using a multipinhole design or multihead structure. Spatial resolution of U-SPECT II for Tc-99m using 0.6 and 0.35 mm pinholes is about 0.35 and 0.3 mm, respectively. The nanoScan system provides 0.85 and 1.4 mm spatial resolution using basic multipinhole collimators for mouse and rat imaging, respectively. Spatial resolution of the PERSPECT using FABCP image reconstruction algorithm is about 0.3 mm in ideal point source examination and about 0.6 mm in micro-Derenzo simulations.

5. CONCLUSION

A dedicated small-animal SPECT imaging system with a novel geometry and data acquisition was introduced in this work. The particular structure of the system design enables desktop open-gantry imaging. In addition, a dedicated image reconstruction algorithm, FABCP, was developed. The results based on MC and analytical simulations showed that the system depicted high spatial resolution and appropriate sensitivity (207 cps/MBq), while the novel concept enables potentially major ease of application due to its desktop open-gantry configuration, low fabrication/service expenses, and mechanical stability, all favorable factors in preclinical SPECT system.

CONFLICT OF INTEREST DISCLOSURE

The authors have no COI to report.

a)Author to whom correspondence should be addressed. Electronic mail: mohammadreza_ay@sina.tums.ac.ir; Telephone/Fax: +982166907532.
[1]M. M. Khalil, J. L. Tremoleda, T. B. Bayomy, and W. Gsell, "Molecular SPECT imaging: An overview," Int. J. Mol. Imaging **2011**, 1–15.
[2]G. K. Loudos *et al.*, "A 3D high-resolution gamma camera for radiopharmaceutical studies with small animals," Appl. Radiat. Isot. **58**, 501–508 (2003).
[3]G. K. Loudos *et al.*, "Improving spatial resolution in SPECT with the combination of PSPMT based detector and iterative reconstruction algorithms," Comput. Med. Imaging Graphics **27**, 307–313 (2003).
[4]A. G. Weisenberger *et al.*, Presented at the IEEE Nuclear Science Symposium Conference Record, 2004.
[5]E. Lage *et al.*, Presented at the IEEE Nuclear Science Symposium Conference Record, 2007.
[6]S. Sajedi *et al.*, "Design and development of a high resolution animal SPECT scanner dedicated for rat and mouse imaging," Nucl. Instrum. Methods Phys. Res., Sect. A **741**, 169–176 (2014).
[7]A. M. Pashazadeh *et al.*, "Experimental evaluation of the performance of HiReSPECT scanner: A high-resolution SPECT system for small animal imaging," Front. Biomed. Technol. **1**, 222–227 (2014).
[8]V. Moji *et al.*, "Performance evaluation of a newly developed high-resolution, dual-head animal SPECT system based on the NEMA NU1-2007 standard," J. Appl. Clin. Med. Phys. **15**, 267–278 (2014).
[9]P. Russo and A. Del Guerra, "Solid-state detectors for small-animal imaging," in *Molecular Imaging of Small Animals*, edited by H. Zaidi (Springer, New York, NY, 2014), pp. 23–82.
[10]W. Choong, W. W. Moses, C. S. Tindall, and P. N. Luke, Presented at the IEEE Nuclear Science Symposium Conference Record, 2003.
[11]S. Shokouhi, B. S. McDonald, H. L. Durko, M. A. Fritz, L. R. Furenlid, and T. E. Peterson, "Thick silicon double-sided strip detectors for low-energy small-animal SPECT," IEEE Trans. Nucl. Sci. **56**, 557–564 (2009).
[12]N. Kubo *et al.*, "Evaluating performance of a pixel array semiconductor SPECT system for small animal imaging," Ann. Nucl. Med. **19**, 633–639 (2005).
[13]Y. Higaki, M. Kobayashi, T. Uehara, H. Hanaoka, Y. Arano, and K. Kawai, "Appropriate collimators in a small animal SPECT scanner with CZT detector," Ann. Nucl. Med. **27**, 271–278 (2013).
[14]C. Damiani, G. Di Domenico, E. Moretti, N. Sabba, G. Zavattini, and A. Del Guerra, Presented at the IEEE Nuclear Science Symposium Conference Record, 2002.
[15]G. L. Zeng, "A skew-slit collimator for small-animal SPECT," J. Nucl. Med. Technol. **36**, 207–212 (2008).
[16]S. Walrand, F. Jamar, M. de Jong, and S. Pauwels, "Evaluation of novel whole-body high-resolution rodent SPECT (linoview) based on direct acquisition of linogram projections," J. Nucl. Med. **46**, 1872–1880 (2005).
[17]T. Zeniya *et al.*, "Use of a compact pixellated gamma camera for small animal pinhole SPECT imaging," Ann. Nucl. Med. **206**, 409–416 (2006).
[18]S. Metzler, S. Vemulapalli, R. Jaszczak, G. Akabani, and B. Chin, "Feasibility of whole-body functional mouse imaging using helical pinhole SPECT," Mol. Imaging Biol. **12**, 35–41 (2010).
[19]A. Rahmim and H. Zaidi, "PET versus SPECT: Strengths, limitations and challenges," Nucl. Med. Commun. **29**, 193–207 (2008).
[20]L. R. Furenlid *et al.*, "FastSPECT II: A second-generation high-resolution dynamic SPECT imager," IEEE Trans. Nucl. Sci. **51**, 631–635 (2004).
[21]F. van der Have, B. Vastenhouw, M. Rentmeester, and F. J. Beekman, "System calibration and statistical image reconstruction for ultra-high resolution stationary pinhole SPECT," IEEE Trans. Med. Imaging **27**, 960–971 (2008).
[22]F. van der Have *et al.*, "U-SPECT-II: An ultra-high-resolution device for molecular small-animal imaging," J. Nucl. Med. **50**, 599–605 (2009).
[23]B. W. Miller, L. R. Furenlid, S. K. Moore, H. B. Barber, V. V. Nagarkar, and H. H. Barrett, "System integration of FastSPECT III, a

dedicated SPECT rodent-brain imager based on BazookaSPECT detector technology," in *IEEE Nuclear Science Symposium Conference Record* (IEEE, 2009), pp. 4004–4008.

[24]H. Hsieh and I. Hsiao, "Image reconstructions from limit views and angle coverage data for a stationary multi-pinhole SPECT system," Tsinghua Sci. Technol. **15**, 44–49 (2010).

[25]S. Shokouhi, D. W. Wilson, S. D. Metzler, and T. E. Peterson, "Evaluation of image reconstruction for mouse brain imaging with synthetic collimation from highly multiplexed SiliSPECT projections," Phys. Med. Biol. **55**, 5151–5168 (2010).

[26]R. J. Havelin *et al.*, "Design and performance of a small-animal imaging system using synthetic collimation," Phys. Med. Biol. **58**, 3397–3412 (2013).

[27]A. Z. Kyme, V. W. Zhou, S. R. Meikle, and R. R. Fulton, "Real-time 3D motion tracking for small animal brain PET," Phys. Med. Biol. **53**, 2651–2666 (2008).

[28]A. G. Weisenberger *et al.*, Presented at the IEEE Nuclear Science Symposium Conference Record, 2008.

[29]J. S. Baba *et al.*, "Molecular imaging of conscious, unrestrained mice with AwakeSPECT," J. Nucl. Med. **54**, 969–976 (2013).

[30]H. Zaidi, "Monte Carlo modeling in nuclear medicine imaging," in *Quantitative Analysis in Nuclear Medicine Imaging*, edited by H. Zaidi (Springer, Singapore, 2006).

[31]G. S. Mitchell and S. R. Cherry, "A high-sensitivity small animal SPECT system," Phys. Med. Biol. **54**, 1291–1305 (2009).

[32]T. E. Peterson, S. Shokouhi, L. R. Furenlid, and D. W. Wilson, "Multi-pinhole SPECT imaging with silicon strip detectors," IEEE Trans. Nucl. Sci. **56**, 646–652 (2009).

[33]S. Shokouhi, S. D. Metzler, D. W. Wilson, and T. E. Peterson, "Multi-pinhole collimator design for small-object imaging with SiliSPECT: A high-resolution SPECT," Phys. Med. Biol. **54**, 207–225 (2009).

[34]N. Zeraatkar, M. Ay, A. Kamali-Asl, and H. Zaidi, "Accurate Monte Carlo modeling and performance assessment of the X-PET™ subsystem of the FLEX Triumph™ preclinical PET/CT scanner," Med. Phys. **38**, 1217–1225 (2011).

[35]H. Mahani, A. Kamali-Asl, and M. R. Ay, "How gamma camera's head-tilts affect image quality of a nuclear scintigram?," Front. Biomed. Technol. **1**, 265–270 (2014).

[36]C.-H. Hsu and P.-C. Huang, "A geometric system model of finite aperture in small animal pinhole SPECT imaging," Comput. Med. Imaging Graphics **30**, 181–185 (2006).

[37]S. Y. Chun, J. A. Fessler, and Y. K. Dewaraja, "Correction for collimator-detector response in SPECT using point spread function template," IEEE Trans. Med. Imaging **32**, 295–305 (2013).

[38]V. Bom, M. Goorden, and F. Beekman, "Comparison of pinhole collimator materials based on sensitivity equivalence," Phys. Med. Biol. **56**, 3199–3214 (2011).

[39]N. Zeraatkar, M. Ay, P. Ghafarian, S. Sarkar, P. Geramifar, and A. Rahmim, "Monte Carlo-based evaluation of inter-crystal scatter and penetration in the PET subsystem of three GE discovery PET/CT scanners," Nucl. Instrum. Methods Phys. Res., Sect. A **659**, 508–514 (2011).

[40]G. S. Mok, Y. Wang, and B. M. Tsui, "Quantification of the multiplexing effects in multi-pinhole small animal SPECT: A simulation study," IEEE Trans. Nucl. Sci. **56**, 2636–2643 (2009).

[41]X. Zhang and Y. Qi, "An analytical simulation technique for cone-beam CT and pinhole SPECT," Nucl. Sci. Tech. **22**, 338–343 (2011).

[42]P. E. B. Vaissier, M. C. Goorden, B. Vastenhouw, F. van der Have, R. M. Ramakers, and F. J. Beekman, "Fast spiral SPECT with stationary γ-cameras and focusing pinholes," J. Nucl. Med. **53**, 1292–1299 (2012).

[43]P. Aguiar *et al.*, "Analytical, experimental, and Monte Carlo system response matrix for pinhole SPECT reconstruction," Med. Phys. **41**, 032501 (10pp.) (2014).

[44]S. Jan, G. Santin, D. Strul, S. Staelens, K. Assié, D. Autret, S. Avner, R. Barbier, M. Bardies, P. M. Bloomfield, D. Brasse, V. Breton, P. Bruyndonckx, I. Buvat, A. F. Chatziioannou, Y. Choi, Y. H. Chung, C. Comtat, D. Donnarieix, L. Ferrer, S. J. Glick, C. J. Groiselle, D. Guez, P. F. Honore, S. Kerhoas-Cavata, A. S. Kirov, V. Kohli, M. Koole, M. Krieguer, D. J. van der Laan, F. Lamare, G. Largeron, C. Lartizien, D. Lazaro, M. C. Maas, L. Maigne, F. Mayet, F. Melot, C. Merheb, E. Pennacchio, J. Perez, U. Pietrzyk, F. R. Rannou, M. Rey, D. R. Schaart, C. R. Schmidtlein, L. Simon, T. Y. Song, J. M. Vieira, D. Visvikis, R. Van de Walle, E. Wiers, and C. Morel, "Gate: A simulation toolkit for PET and SPECT," Phys. Med. Biol. **49**, 4543–4561 (2004).

[45]S. Jan, D. Benoit, E. Becheva, T. Carlier, F. Cassol, P. Descourt, T. Frisson, L. Grevillot, L. Guigues, L. Maigne, C. Morel, Y. Perrot, N. Rehfeld, D. Sarrut, D. R. Schaart, S. Stute, U. Pietrzyk, D. Visvikis, N. Zahra, and I. Buvat, "GATE V6: A major enhancement of the GATE simulation platform enabling modelling of CT and radiotherapy," Phys. Med. Biol. **56**, 881–901 (2011).

[46]W. P. Segars, B. M. W. Tsui, E. C. Frey, G. A. Johnson, and S. S. Berr, "Development of a 4D digital mouse phantom for molecular imaging research," Mol. Imaging Biol. **6**, 149–159 (2004).

[47]A. P. Dempster, N. M. Laird, and D. B. Rdin, "Maximum likelihood from incomplete data via the EM algorithm," J. R. Stat. Soc., Ser. B **39**, 1–38 (1977).

[48]L. A. Shepp and Y. Vardi, "Maximum likelihood reconstruction for emission tomography," IEEE Trans. Med. Imaging **1**, 113–122 (1982).

[49]R. Accorsi and S. D. Metzler, "Analytic determination of the resolution-equivalent effective diameter of a pinhole collimator," IEEE Trans. Med. Imaging **23**, 750–763 (2004).

[50]R. Accorsi and S. D. Metzler, "Resolution-effective diameters for asymmetric-knife-edge pinhole collimators," IEEE Trans. Med. Imaging **24**, 1637–1646 (2005).

[51]Y. Takahashi, K. Murase, T. Mochizuki, H. Higashino, Y. Sugawara, and A. Kinda, "Evaluation of the number of SPECT projections in the ordered subsets-expectation maximization image reconstruction method," Ann. Nucl. Med. **17**, 525–530 (2003).

[52]S. Agostinelli *et al.*, "Geant4—A simulation toolkit," Nucl. Instrum. Methods Phys. Res., Sect. A **506**, 250–303 (2003).

[53]J. R. Mallard and M. J. Myers, "The performance of a gamma camera for the visualization of radioactive isotopes *in vivo*," Phys. Med. Biol. **8**, 165–182 (1963).

[54]H. O. Anger, "Radioisotope cameras," Instrum. Nucl. Med. **1**, 485–552 (1967).

[55]D. Paix, "Pinhole imaging of gamma rays," Phys. Med. Biol. **12**, 489–500 (1967).

[56]S. D. Metzler, J. E. Bowsher, M. F. Smith, and R. J. Jaszczak, "Analytic determination of pinhole collimator sensitivity with penetration," IEEE Trans. Med. Imaging **20**, 730–741 (2001).

[57]S. D. Metzler and R. Accorsi, "Resolution- versus sensitivity-effective diameter in pinhole collimation: Experimental verification," Phys. Med. Biol. **50**, 5005–5017 (2005).

[58]E. C. Frey and B. M. W. Tsui, "Collimator-detector response compensation in SPECT," in *Quantitative Analysis in Nuclear Medicine Imaging*, edited by H. Zaidi (Springer, Singapore, 2006).

[59]H.-H. Lee and J.-C. Chen, "Investigation of attenuation correction for small-animal single photon emission computed tomography," Comput. Math. Methods Med. **2013**, 430276.

[60]H. Jacobowitz and S. D. Metzler, "Geometric sensitivity of a pinhole collimator," Int. J. Math. Math. Sci. **2010**, 1–18.

[61]F. J. Beekman *et al.*, "U-SPECT-I: A novel system for submillimeter-resolution tomography with radiolabeled molecules in mice," J. Nucl. Med. **46**, 1194–1200 (2005).

[62]F. P. Difilippo, "Design and performance of a multi-pinhole collimation device for small animal imaging with clinical SPECT and SPECT-CT scanners," Phys. Med. Biol. **53**, 4185–4201 (2008).

[63]J. Mejia, O. Y. Galvis-Alonso, A. A. Castro, J. Braga, J. P. Leite, and M. V. Simoes, "A clinical gamma camera-based pinhole collimated system for high resolution small animal SPECT imaging," Braz. J. Med. Biol. Res. **43**, 1160–1166 (2010).

[64]E. C. Frey and B. M. W. Tsui, "Collimator-detector response compensation in SPECT," in *Quantitative Analysis in Nuclear Medical Imaging*, edited by H. Zaidi (Springer, New York, NY, 2006).

[65]N. Zeraatkar *et al.*, "Resolution-recovery-embedded image reconstruction for a high-resolution animal SPECT system," Phys. Med. **30**, 774–781 (2014).

[66]H. K. Tuy, "An inversion formula for cone-beam reconstruction," SIAM J. Appl. Math. **43**, 546–552 (1983).

[67]S. D. Metzler, J. E. Bowsher, and R. J. Jaszczak, "Geometrical similarities of the Orlov and Tuy sampling criteria and a numerical algorithm for assessing sampling completeness," IEEE Trans. Nucl. Sci. **50**, 1550–1555 (2003).

[68]B. C. Yoder, Ph.D. Thesis, University of North Carolina, 2008.

[69]Mediso-Medical-Imaging-Systems, nanoScan Family, Preclinical SPECT Imaging Systems [catalog], 2013.